Kenneth N. Aycock[1]
Bioelectromechanical Systems Lab,
Virginia Tech—Wake Forest School of
Biomedical Engineering and Sciences,
Virginia Tech Department of Biomedical
Engineering and Mechanics,
320 Kelly Hall,
325 Stanger Street,
Blacksburg, VA 24061
e-mail: kna@vt.edu

Sabrina N. Campelo
Bioelectromechanical Systems Lab,
Virginia Tech—Wake Forest School of
Biomedical Engineering and Sciences,
Virginia Tech Department of Biomedical
Engineering and Mechanics,
320 Kelly Hall,
325 Stanger Street,
Blacksburg, VA 24061
e-mail: scampelo@vt.edu

Rafael V. Davalos
ASME Fellow
Bioelectromechanical Systems Lab,
Virginia Tech—Wake Forest School of
Biomedical Engineering and Sciences,
Virginia Tech Department of Biomedical
Engineering and Mechanics,
320 Kelly Hall,
325 Stanger Street,
Blacksburg, VA 24061
e-mail: davalos@vt.edu

A Comparative Modeling Study of Thermal Mitigation Strategies in Irreversible Electroporation Treatments
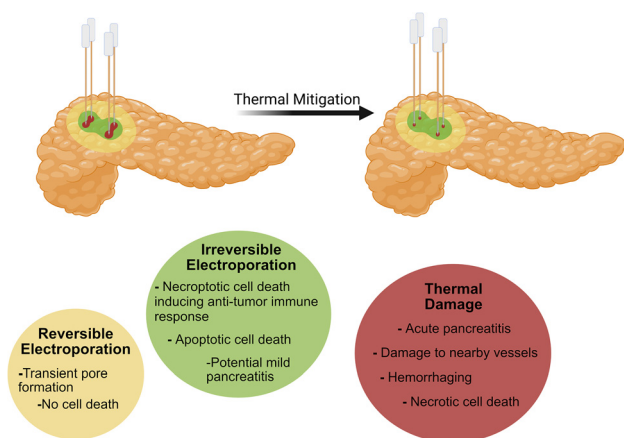
Irreversible electroporation (IRE), also referred to as nonthermal pulsed field ablation (PFA), is an attractive focal ablation modality for solid tumors and cardiac tissue due to its ability to destroy aberrant cells with limited disruption of the underlying tissue architecture. Despite its nonthermal cell death mechanism, application of electrical energy results in Joule heating that, if ignored, can cause undesired thermal injury. Engineered thermal mitigation (TM) technologies including phase change materials (PCMs) and active cooling (AC) have been reported and tested as a potential means to limit thermal damage. However, several variables affect TM performance including the pulsing paradigm, electrode geometry, PCM composition, and chosen active cooling parameters, meaning direct comparisons between approaches are lacking. In this study, we developed a computational model of conventional bipolar and monopolar probes with solid, PCM-filled, or actively cooled cores to simulate clinical IRE treatments in pancreatic tissue. This approach reveals that probes with integrated PCM cores can be tuned to drastically limit thermal damage compared to existing solid probes. Furthermore, actively cooled probes provide additional control over thermal effects within the probe vicinity and can altogether abrogate thermal damage. In practice, such differences in performance must be weighed against the increased time, expense, and effort required for modified probes compared to existing solid probes. [DOI: 10.1115/1.4053199]

Introduction

Irreversible electroporation (IRE), or nonthermal pulsed field ablation (PFA), is a focal tissue ablation modality used to treat solid tumors and arrhythmogenic cardiac tissue [1,2]. IRE is performed by applying a series of short (1–100 μs), high intensity (1–3 kV/cm) electrical pulses to elevate the transmembrane potential (TMP) of cells within the targeted region beyond a threshold value (~1 V). Once this threshold is exceeded, nanoscale defects—or "pores"—appear in the cellular membrane [3,4]. When several pulses of sufficient magnitude are applied, formation of large, long-lived pores leads to disruption of cellular homeostasis, eventually causing death through various pathways [1,5,6]. Due to cell death relying solely on the induced TMP, IRE is considered a nonthermal ablation modality; thus, it can be employed in various scenarios where thermal ablation is contraindicated [7,8]. This includes deep-seated tumors situated near vascular and/or neural structures [9,10], as well as sensitive myocardial tissue in which thermal ablation is associated with numerous side effects [11].

In oncology, IRE is administered through two (or more) needle electrodes inserted directly into the targeted region containing the tumor prior to pulse delivery. In select instances, a single-insertion bipolar probe (two electrodes integrated within the same cylindrical shaft) is used [12,13]. For each treatment, the type and number of electrodes, as well as their spacing and exposure, are carefully selected to ensure the targeted region is exposed to an electric field of sufficient strength to induce cell death. Although IRE relies on a nonthermal mechanism, ablating the desired treatment region with zero thermal damage can sometimes be challenging (Fig. 1).

Fig. 1 If not actively considered in treatment planning and delivery, irreversible electroporation can result in thermal damage, which can cause undesirable side effects. The use of thermal mitigation strategies reduces the likelihood of thermal damage, minimizing the risk of adverse effects and improving control over expected cell death mechanisms.

The first modeling study on IRE showed that ablation and thermal effects can be mutually exclusive phenomena within certain constraints, and countless follow-up studies have determined optimal parameters for ablation in different settings [14]. However, undesired side effects due to temperature development remain the foremost factor limiting the size of IRE ablations [15,16]. Clinically, differences in institutional pulse administration protocols and clinician experience can generate varying degrees of thermal tissue injury, which are likely somewhat responsible for the range of complication rates and oncological outcomes reported in the literature [13,17–19]. Even with moderate voltages, the steep potential gradient at the electrode boundaries can produce relatively high electric fields (and thus, temperatures), leading to effects such as tissue coagulation, denaturation of extracellular proteins, and hemorrhage [20]. In rare cases, significant increases in electrical current due to heating can pose the risk of electrical arcing [21,22].

Despite these concerns, existing clinical pulsing protocols do not actively consider temperature rise during IRE procedures. In the absence of real-time feedback during pulse delivery, the risk of thermal damage can vary widely between patients depending upon the tissue being treated, electrode configuration and pulsing paradigm, as well as patient-specific tissue properties [23,24]. For example, a recent study estimated that approximately 30% of the average IRE ablation volume experiences mild hyperthermia (40–50 °C), with 5% being exposed to temperatures in excess of 50 °C [18]. As clinicians and researchers continually seek to expand ablation volumes toward treating larger tumors, maintaining the nonthermal aspects of IRE will be increasingly difficult [25]. Additionally, recent work suggests that even when thermal damage is unlikely, reducing mild-to-moderate thermal effects could promote better immune activation [5,26], which could enhance long-term treatment efficacy and lead to improved patient outcomes [27,28]. Thus, solutions to mitigate and/or control thermal effects in the vicinity of the electrodes are paramount to optimizing IRE and other pulsed electric field (PEF)-based ablation modalities for more widespread clinical adoption.

Several approaches to limit temperature rise during PEF therapies—termed thermal mitigation (TM) strategies—have been considered. These include innovative probe designs that integrate heat-dissipating technologies as well as pulse paradigm adjustments that allow tissue perfusion to disperse heat between consecutive pulses. Prior work has examined the feasibility of actively perfusing a cooling solution through a bipolar probe [29], integrating phase change materials (PCMs) [30,31] or an endothermic reaction [32] within the core of monopolar probes, and distributing applied energy into "cycles" where a subset of pulses is delivered across each electrode pair repeatedly until the total number of pulses is reached [23]. A summary of these strategies, along with advantages and drawbacks of each, can be found in Table 1.

Notably, each of these prior investigations was performed independently, so it remains relatively unknown how different TM strategies compare to one another. In this study, we numerically compare the utility of two engineered TM strategies that have been introduced and examined experimentally, as these are the technologies most likely to be adopted in medical practice. To build a more comprehensive understanding of how these TM technologies may perform in clinical scenarios, we determine treatment conditions where thermal mitigation approaches are necessary, then assess design and performance characteristics that may affect the efficacy of either technology.

Methods

General Model Construction. Numerical simulations were performed in COMSOL MULTIPHYSICS 5.6 (Comsol, Stockholm, Sweden) to determine the electric field and temperature distributions arising from a clinical procedure performed with various electrode types. For simulations considering a single bipolar probe, a 2D axisymmetric model was used to reduce computation time. For all other simulations, a 3D model was used. In all cases, pancreatic tissue was represented by an ellipsoid with dimensions of 15 cm × 15 cm × 25 cm. These dimensions were chosen to prevent boundary effects while also allowing for an identical modeling domain between 2D axisymmetric and 3D simulations. Electrical field distribution and thermal effects were computed using common techniques [33,34]. Briefly, the electric potential distribution at the end of a given pulse was calculated using a modified Laplace equation under the electroquasistatic approximation (Eq. (1)), and the resulting electric field distribution with Eq. (2)

$$-\nabla \cdot (\sigma(|E|, T)\nabla\Phi) = 0 \qquad (1)$$

$$\vec{E} = -\nabla\Phi \qquad (2)$$

where σ is the electrical conductivity, which depends on both the local field magnitude $|E|$ and temperature T, and Φ is the local electric potential. Equation (1) is valid given that the pulse width is much longer than the charging time constant of cell membranes

Table 1   Summary of previously introduced thermal mitigation strategies

Modality	Configuration	Mode of action	Advantages	Drawbacks	References
Active cooling (AC)	Bipolar	– Applicator is cooled internally with water perfusion	– Efficient reduction of tissue temperature	– Cumbersome electrode – Requires external equipment – May require more fixation devices	[29]
Phase change material (PCM)	Monopolar	– Heat absorbed due to phase change of embedded material	– Moderate reduction in temperature - No change to clinical procedure	– Limited by choice of PCM – Finite duration in which heat is absorbed	[30,31]
Cycled pulsing	Monopolar	– Reduced number of contiguous pulses across a single electrode pair	– Simple change to pulsing paradigm that can limit temperature rise due to cumulative pulses	– Only applicable to multi-electrode experiments – Potential increase in procedure duration	[23]
Endothermic reaction	Monopolar	– Heat absorbed due to endothermic processes	– No changes to clinical procedure - Efficient reduction in temperature rise for a short time	– Not reduced to practice – Potentially complicated to design/implement	[32]

Table 2   Material properties used in each modeling domain for solid-core electrodes

Material	Symbol	Description	Value	Units	References
Stainless steel					
	ρ	Mass density	7900	$\mathrm{kg\,m^{-3}}$	[29]
	σ	Electrical conductivity	2.22×10^6	$\mathrm{S\,m^{-1}}$	[29]
	k	Thermal conductivity	15	$\mathrm{W\,m^{-1}\,K^{-1}}$	[29]
	c_p	Heat capacity	500	$\mathrm{J\,kg^{-1}\,K^{-1}}$	[29]
Insulation					
	ρ	Mass density	2329	$\mathrm{kg\,m^{-3}}$	[29]
	σ	Electrical conductivity	1×10^{-12}	$\mathrm{S\,m^{-1}}$	[29]
	k	Thermal conductivity	0.2	$\mathrm{W\,m^{-1}\,K^{-1}}$	[39]
	c_p	Heat capacity	700	$\mathrm{J\,kg^{-1}\,K^{-1}}$	[29]
Pancreatic tissue					
	ρ	Mass density	1087	$\mathrm{kg\,m^{-3}}$	[40]
	σ_0	Baseline electrical conductivity	0.118	$\mathrm{S\,m^{-1}}$	[38]
	σ_f	Final electrical conductivity	0.268	$\mathrm{S\,m^{-1}}$	[38]
	A	Fitting parameter	2.5×10^{-3}	$\mathrm{cm\,V^{-1}}$	[38]
	E_{del}	Transition zone midpoint	1738	$\mathrm{V\,cm^{-1}}$	[38]
	α	Conductivity thermal coefficient	0.02	$\mathrm{^\circ C^{-1}}$	[38]
	a	Linear fitting parameter	5.7×10^{-4}	$\mathrm{W\,m^{-1}\,K^{-2}}$	[35]
	b	Baseline thermal conductivity	0.506	$\mathrm{W\,m^{-1}\,K^{-1}}$	[35]
	c_p	Heat capacity	3164	$\mathrm{J\,kg^{-1}\,K^{-1}}$	[40]
	ω_b	Average blood perfusion rate	1.39×10^{-2}	$\mathrm{s^{-1}}$	[40]
	ρ_b	Blood density	1050	$\mathrm{kg\,m^{-3}}$	[40]
	$c_{p,b}$	Blood heat capacity	3617	$\mathrm{J\,kg^{-1}\,K^{-1}}$	[40]

($\sim 1 \ \mu$s). One electrode boundary was set to $\Phi = V_0$ and the other set to $\Phi = 0$. External boundaries were considered insulating to provide a worst-case approximation to thermal effects. After computing the field distribution, tissue temperature was calculated using the traditional Pennes bioheat equation with the addition of a Joule heating term Q_J

$$\rho c_p \frac{\partial T}{\partial t} = \nabla \cdot (k(T)\nabla T) + \rho_b c_{p,b}\omega_b(T_b - T) + Q_J \qquad (3)$$

Here, ρ and c_p are the tissue density and heat capacity, respectively, and ρ_b and $c_{p,b}$ are the same for blood; ω_b is the blood perfusion rate; T_b is the temperature of blood (37 °C); and tissue thermal conductivity, $k(T)$, was taken to have a linear dependence on local temperature and computed as

$$k(T) = a \cdot T + b \qquad (4)$$

where a and b are empirically determined fitting coefficients [35]. Initially, all domains were set to physiologic temperature (37 °C), and all external boundaries were considered adiabatic unless otherwise indicated. The Joule heating term was calculated in all domains as

$$Q_J = \sigma|E|^2 \qquad (5)$$

and was scaled by the duty cycle—the product of pulse duration and pulse frequency—as previously described [36]. Electroporation results in a field-dependent increase in electrical conductivity due to intra- and extracellular exchange of ions, and thermal effects cause further increases at a rate of $\sim$1–2%/°C. These effects are captured through the following expression:

$$\sigma(|E|,T) = \left[\sigma_0 + \frac{\sigma_f - \sigma_0}{1 + e^{-A\cdot(|E|-E_{\mathrm{del}})}}\right](1 + \alpha(T - T_0)) \qquad (6)$$

where σ_0 is the baseline electrical conductivity, σ_f is the maximum (electroporated) conductivity, A is a fitting parameter determining how quickly the conductivity transitions from its native state to fully electroporated, E_{del} is the midpoint of the transition,

α is the thermal coefficient of conductivity, and T_0 is the baseline temperature at which σ_0 was determined.

Finally, thermal damage in the tissue domain was calculated with an Arrhenius-type dose equation based on the temperature over time at each point

$$\Omega = \int \xi e^{-E_a/(R\cdot T(t))}dt \qquad (7)$$

where Ω is the Arrhenius damage integral, ξ is the frequency factor, E_a is the activation energy, R is the gas constant, and $T(t)$ is the temperature at time t. Tissue exposed to Ω values of 0.53 or greater was assumed to be thermally damaged, as this has been empirically estimated as the onset of irreversible thermal damage in blood-perfused skin [37].

Unless otherwise indicated, tissue was modeled as pancreas and assigned previously published dynamic electrical conductivity parameters [38]. Properties assigned to each domain can be found in Table 2.

Phase Change Material. Latent heat storage systems rely on PCMs to store thermal energy for various applications. Due to their high latent heat of fusion, PCMs absorb energy as they transition from solid (*s*) to liquid (*l*) while maintaining a nearly constant temperature. In other words, when heated to their melting point, PCMs require further energy to change phases, and until this phase transition is complete, temperature remains stagnant.

Mathematically, heat absorption during the phase change was modeled with the effective heat capacity $(c_{p,\mathrm{eq}})$ method by including the latent heat of fusion (λ) in the volume average of the specific heat capacity at constant pressure [31]

$$c_{p,\mathrm{eq}} = \Theta(c_{p,s} + \lambda\Pi) + (1 - \Theta)(c_{p,l} + \lambda\Pi) \qquad (8)$$

where Θ is the volume fraction of solid PCM, computed as

$$\Theta = 1 - flc2hs[(T - T_m), T_R] \qquad (9)$$

in which *flc2hs* is a Heaviside function centered about the melting temperature (T_M) and stepping from 1 to 0 over the transition range T_R. This function approximates the solid-to-liquid *(s-l)*

Table 3 Material properties and characteristics for actively cooled and PCM-core probes

Strategy	Symbol	Description	Value	Units	References
PCM					
	ρ	Mass density (s/l)	1520/1450	$\mathrm{kg\,m^{-3}}$	[30]
	σ	Electrical conductivity (s/l)	1.0/1.0	$\mathrm{S\,m^{-1}}$	[30]
	k	Thermal conductivity (s/l)	1.0/0.6	$\mathrm{W\,m^{-1}\,K^{-1}}$	[30]
	c_p	Heat capacity (s/l)	1960/3430	$\mathrm{J\,kg^{-1}\,K^{-1}}$	[30]
	λ	Latent heat of fusion	266	$\mathrm{kJ\,kg^{-1}}$	[30]
	T_m	Melting temperature	43	$^\circ$C	—
	dT	Temperature transition range	2	$^\circ$C	—
Active cooling					
	h	Heat transfer coefficient	0.381	$\mathrm{W\,cm^{-2}\,K^{-1}}$	[41,42]
	T_{ext}	Perfusate temperature	37	$^\circ$C	—

transition as a smooth step with a continuous second derivative, reducing computational burden associated with true logical steps. In Eq. (8), Π is a normalized pulse occurring about T_M, calculated by taking the derivative of Θ with respect to T. In the PCM domain, the temperature distribution was calculated in a similar manner to that of the tissue domain but without perfusion (Eq. (10)), and by using the volume averages of either phase to calculate density (ρ_{eq}) and thermal conductivity (k_{eq})

$$(\rho c_p)_{\mathrm{eq}} \frac{\partial T}{\partial t} = \nabla \cdot (k_{\mathrm{eq}} \nabla T) + Q_J \tag{10}$$

$$\rho_{\mathrm{eq}} = \Theta \rho_s + (1 - \Theta) \rho_l \tag{11}$$

$$k_{\mathrm{eq}} = \Theta k_s + (1 - \Theta) k_l \tag{12}$$

Unless explicitly stated, material properties of the PCM were taken from Ref. [30] and are listed in Table 3.

Active Cooling. Active cooling is a technology commonly integrated within the core of delivery devices used for thermal ablation to limit tissue charring immediately adjacent to the probe. The core of the device contains two concentric cylinders such that fluid flows in through the innermost cylinder before exiting via the outer cylinder (Fig. 2). This allows for convective transfer of thermal energy from adjacent tissue to the perfusate, limiting temperature rise near the probe edge.

From a computational perspective, the core of the probe was taken to be hollow, and a convective heat flux was assigned to the perfusion channel boundary within the probe

$$-k \cdot \nabla T = h \cdot (T - T_{\mathrm{ext}}) \tag{13}$$

where h is the heat transfer coefficient, T is the electrode temperature at the boundary, and T_{ext} is the perfusate temperature. The convective heat transfer coefficient was computed as previously described and was found to be similar to values reported in prior works with comparable channel geometries and flow characteristics [41,42]. Briefly, the user-defined volumetric flow rate, along with the diameter (D) of the perfusion inlet, was used to compute the fluid velocity within the electrode shaft $\left(V = \frac{Q}{A}\right)$. Next, assuming material properties of water, Reynolds (Re) and Prandtl (Pr) number were computed (Eqs. (14) and (15)). Nusselt number (Nu) for laminar flow within a pipe (Re < 2100) was then calculated using Eq. (16), and from this h was determined (Eq. (17))

$$\mathrm{Re} = \frac{\rho \cdot V \cdot D}{\mu} \tag{14}$$

$$\mathrm{Pr} = \frac{c_p \cdot \mu}{k} \tag{15}$$

$$\mathrm{Nu} = 1.86 \cdot \mathrm{Re}^{1/3} \cdot \mathrm{Pr}^{1/3} \cdot \left(\frac{D}{L}\right)^{1/3} \left(\frac{\mu_b}{\mu_w}\right)^{0.14} \tag{16}$$

$$h = \frac{\mathrm{Nu} \cdot k}{D} \tag{17}$$

In the above equations, ρ, μ, c_p, and k are the density, dynamic viscosity, heat capacity, and thermal conductivity of water, respectively; L is the length of the probe, and μ_b and μ_w are the bulk and wall viscosity of the perfusate. In this work, μ_b/μ_w was assumed to be unity given the relatively low temperatures involved. Perfusate characteristics are given in Table 3.
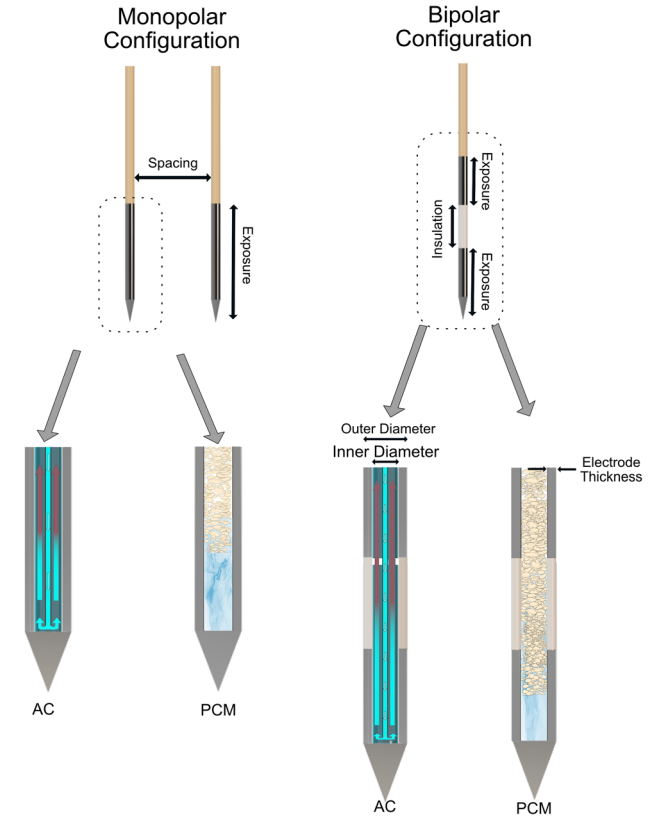
Fig. 2 Schematic diagram of (left) monopolar and (right) bipolar probe geometries employed in numerical models. In standard simulations, center-to-center spacing was 1.5 cm, probe diameter was 1.65 mm, and wall thickness was 0.2 mm for either configuration. For the bipolar configuration, electrode exposure was 7 mm, and insulation height was 8 mm. For monopolar simulations, electrode exposure was 1 cm. A preliminary modeling study was used to ensure that either configuration resulted in similar volumetric exposure to electric fields of 0–2500 V/cm along with similar ablation volumes (data not shown).
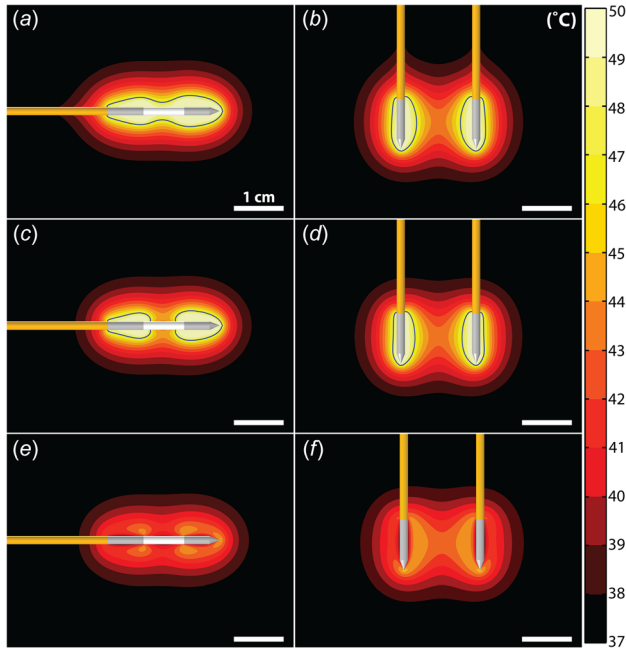
Fig. 3 Temperature distribution at the end of IRE treatment with various probe types and geometries. The left column represents a bipolar probe with a (*a*) solid core, (*c*) PCM-filled core, and (*e*) actively cooled core. The right columns illustrate the same for monopolar probes with (*b*) solid cores, (*d*) PCM-filled cores, and (*f*) actively cooled cores. In panels (*a*)–(*d*), contour line indicates thermal damage ($\Omega > 0.53$), taken 2 min after treatment completion.

Modeling Approach. In both models, a voltage-to-distance ratio of 1500 V/cm was applied across either the bipolar or monopolar configuration (Fig. 2). Unless otherwise specified, simulated treatments consisted of 100 pulses, each with a duration of 100 μs, delivered at a rate of 1 pulse per second. Except where explicitly noted, probes were modeled after existing clinical devices [43]. The bipolar probe was assigned a diameter of 1.65 mm, a wall thickness of 0.2 mm, an electrode exposure of 7 mm (each), and an insulation height of 8 mm. Monopolar probes were given the same diameter and wall thickness, but the exposure was set to 1 mm to coincide with demarcations on commercially available devices.

First, clinically relevant variables expected to impact temperature rise were swept to determine the performance of different integrated TM technologies under these conditions. To illustrate this, pulse rate was selected, as it fluctuates from patient to patient depending on their heart rate and plays a major role in temperature development. Next, geometric parameters were assessed to determine impact of probe geometry on performance. Finally, we parametrically studied the effects of different PCM material properties and active cooling flow characteristics.

Initially, the mesh was refined until less than a 1% difference in electric field distribution along the x-axis was achieved, which resulted in COMSOL's default "extra fine" meshing option. All models were computed on a Dell Optiplex 7071 (Dell Technologies, Round Rock, TX) with eight cores, an Intel Core i9 processor, and 32 GB of RAM. Bipolar models (2D axisymmetric) solved in ~2.5 min while dual monopolar geometries (3D) required ~250 min to solve. For details regarding model validation, please refer to the Supplemental Material, hosted on the ASME Digital Collection.

Results

The temperature distribution during the final pulse of a standard clinical protocol is shown in Fig. 3. Peak temperatures for the
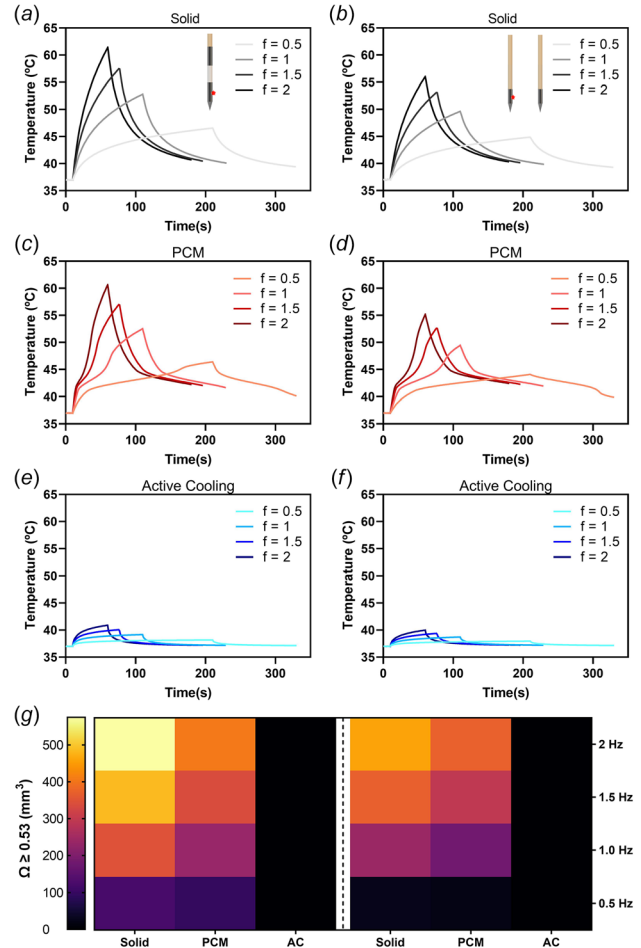
Fig. 4 Impact of pulse delivery rate on temperature rise and thermal damage. Temperature (*a*)–(*f*) at the tissue-electrode boundary is shown for solid (*a*) and (*b*), PCM-filled (*c*) and (*d*), and actively cooled (*e*) and (*f*) probes in either a bipolar (*a*), (*c*), (*e*) or monopolar (*b*), (*d*), (*f*) electrode configuration. Also shown is the (*g*) volume of thermal damage for each case.

bipolar probe are located adjacent to the probe body alongside either electrode, with the distal electrode experiencing marginally more thermal effects than the proximal electrode (Fig. 3(*a*)). Similarly, the monopolar setup exhibited maximum temperatures within the vicinity of the tapered tip, with slightly less thermal damage than corresponding bipolar cases (Fig. 3(*b*)). It is easily observed that probes with integrated TM technologies have reduced thermal damage (contour in Fig. 3) compared to those without, and that active cooling is more effective than PCM (Figs. 3(*c*)–3(*f*)) under these pulse conditions.

To evaluate the significance of pulse delivery rate on performance of PCM or active cooling, a parametric study was performed in which the delivery rate was varied from 1 pulse every 2 s (0.5 Hz) to 2 pulses per second (2 Hz) (Fig. 4). For solid core probes, increasing the delivery rate from 0.5 Hz to 2 Hz correspondingly increased peak temperature at the probe boundary by ~15 °C (Figs. 4(*a*) and 4(*b*)). In the case of PCM-core probes, as temperature approached 43 °C, the integrated PCM absorbed heat, reducing temperature rise by 2–4 °C throughout the treatment duration in both the bipolar (Fig. 4(*c*)) and monopolar (Fig. 4(*d*)) arrangements, resulting in ~2 °C lower peak temperatures compared to the solid probes (Figs. 4(*a*) and 4(*b*)). In comparison to the other probes modeled, temperature in the vicinity of actively cooled probes was relatively unaffected by pulse rate and rose only modestly during treatment; with pulses delivered at 2 Hz, temperature rise was nearly 20 °C less with actively cooled probes
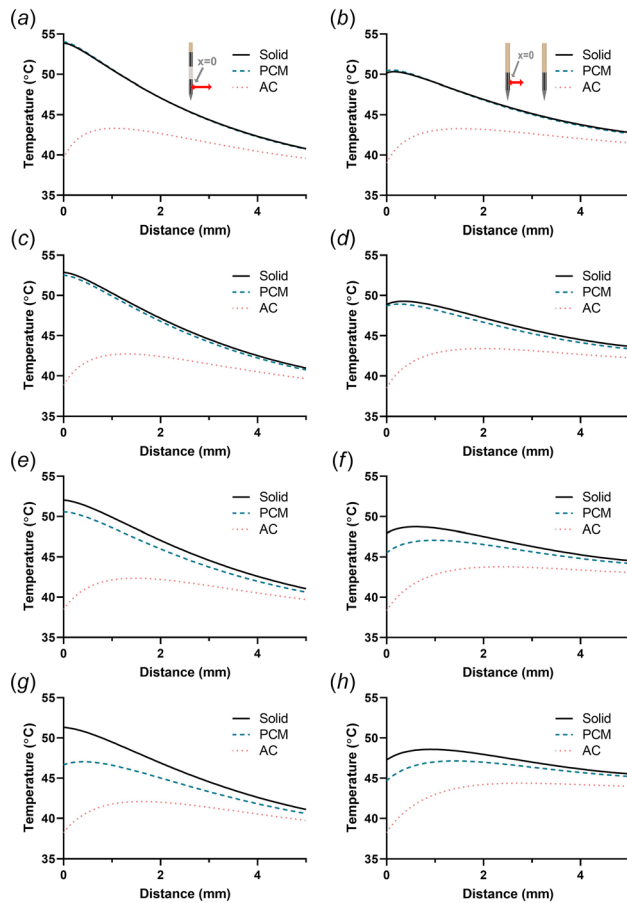
Fig. 5 Probe design affects the performance of PCM-filled probes but not actively cooled probes. Temperature along a line moving radially outward from the electrode edge (*a*)–(*h*) is shown for (*a*), (*c*), (*e*), (*g*) bipolar probes and (*b*), (*d*), (*f*), (*h*) monopolar probes with radii of (*a*) and (*b*) 0.5 mm, (*c*) and (*d*) 0.75 mm, (*e*) and (*f*) 1 mm, and (*g*) and (*h*) 1.25 mm. Center-to-center separation was 1.5 cm for either probe configuration.

relative to the solid counterpart, and other active cooling cases exhibited even less significant thermal effects. These observations are further reflected by the extent of thermal damage. Across all cases, thermal damage volume was reduced by ∼40% with PCM-filled probes compared to solid probes, while actively cooled probes prevented thermal damage altogether (Fig. 4(*g*)).

Next, we examined probe geometry to determine the extent to which design choices might impact the performance of either TM technology. Within either probe type, outer wall thickness was varied from 0.05 mm to 0.3 mm, and diameter from 1 mm to 2.5 mm. For small diameters (1–1.5 mm), there was almost no effect of incorporating PCM into the probe core for either arrangement (Fig. 5). Conversely, temperature reductions appeared when the probe diameter was adjusted to 2 mm, with 2.5 mm offering the most significant benefit. When considering the actively cooled probes, there was not a strong dependence on geometry and in all cases, temperature was highest ∼1 mm from the probe edge with a slight decay thereafter (Fig. 5). Importantly, it appears that integrated TM technologies can impact temperature within ∼4 mm of the edge of bipolar probes and ∼3 mm for monopolar probes, with little change in temperature relative to solid probes thereafter (Fig. 5). In addition to probe diameter, outer wall thickness also played a role in the efficiency of PCM-core probes (Fig. 6) but not actively cooled probes (data not shown). Specifically, wall thickness was especially important for bipolar probes with moderate radii (0.75–1 mm), with thinner walls leading to less thermal

damage (Figs. 6(*a*) and 6(*c*)). In monopolar simulations, probe radius dominated effectiveness of PCM-core electrodes, and wall thickness was not as significant (Figs. 6(*b*) and 6(*d*)).

Finally, we investigated engineering and user-defined parameters that may impact the effectiveness of thermal mitigation strategies (Fig. 7). Because bipolar probes generally resulted in higher temperatures, only this configuration was examined. Additionally, since performance of the PCM-core probes was heavily dependent upon geometry, probe radius for PCM probes was increased to 1 cm, while wall thickness was maintained at 0.2 cm. The standard geometry was employed for actively cooled probes. Figures 7(*a*)–7(*c*) demonstrates that changes to PCM material properties impact its ability to absorb heat during pulse delivery. With a relatively low heat of fusion (Fig. 7(*a*)), tissue temperature is nearly identical regardless of k_{eq}. On the other hand, increasing λ (Figs. 7(*a*)–7(*c*)) has the strongest effect on temperature rise, while k_{eq} had a clear impact when paired with higher values of λ. Of further note, the effect of k_{eq} appeared to plateau once it reached its standard value. For actively cooled probes (Figs. 7(*d*)–7(*f*)) with very low flow rates (i.e., $h/100$), T_{ext} was insignificant (Fig. 7(*d*)). However, by increasing the heat transfer coefficient to $h/10$ (Fig. 7(*e*)), tissue temperature peaked at ∼20–30 °C above T_{ext}. With h set to its baseline value (corresponding to ∼35 mL/min (Fig. 7(*f*))), tissue temperature rapidly approached T_{ext} prior to the onset of pulse application and increased less than 5 °C during treatment.

Discussion

This work modeled and directly compared the theoretical ability of actively cooled and PCM-core electrodes to limit thermal effects during IRE treatment. In addition to IRE, the benefits of integrated TM technologies will translate to other PEF-based ablative and nonablative modalities such as electrochemotherapy (ECT) and electrogene transfer (EGT). Our data demonstrate that the PCM approach was successful in reducing the risk of thermal damage/necrosis, while the actively cooled approach markedly reduced the risk of thermal damage compared to both existing IRE electrodes and PCM-core probes. It is worth mentioning that another engineered strategy, where an endothermic reaction takes place within the probe core during treatment, has been proposed [32]. This design could potentially offer similar or improved performance relative to PCM-core probes within the same platform. However, the endothermic probe has not been fabricated or studied experimentally, and it is not trivial to separate the reactants prior to dissolution. Thus, we chose to omit the endothermic probe from this study.

Throughout this work, actively cooled probes were effective in preventing substantial temperature rise in the vicinity of the electrodes in essentially every case, and no thermal damage was seen except when perfusate temperature was elevated above physiological (body) temperature. This suggests that active cooling is highly efficacious regardless of the probe geometry and pulsing protocol employed. Extrapolating these data implies that tissue conductivity plays only a minor role on the effectiveness of actively cooled probes. Thus, for applications where temperature control and thermal mitigation is an absolute requirement, actively cooled electrodes should be considered. These probes may also be warranted in specific clinical settings during which large ablation volumes are targeted, or when inexperienced users are becoming familiar with IRE and more prone to overtreating. They could also be useful for maintaining tissue temperature at predetermined values during treatment. For instance, perfusate temperature could be held a few degrees above physiologic temperature, as moderate heating has been shown to elicit magnified biophysical effects during certain PEF-based therapies [44,45]. In contrast, with higher flow rates and low perfusate temperatures, although thermal damage becomes a nonissue, ablation size could be negatively affected. Our models predict that with $h = 0.381$ W cm^{-2} K^{-1} and $T_{ext} = 4$ °C, ablation volume would be reduced by 30% versus
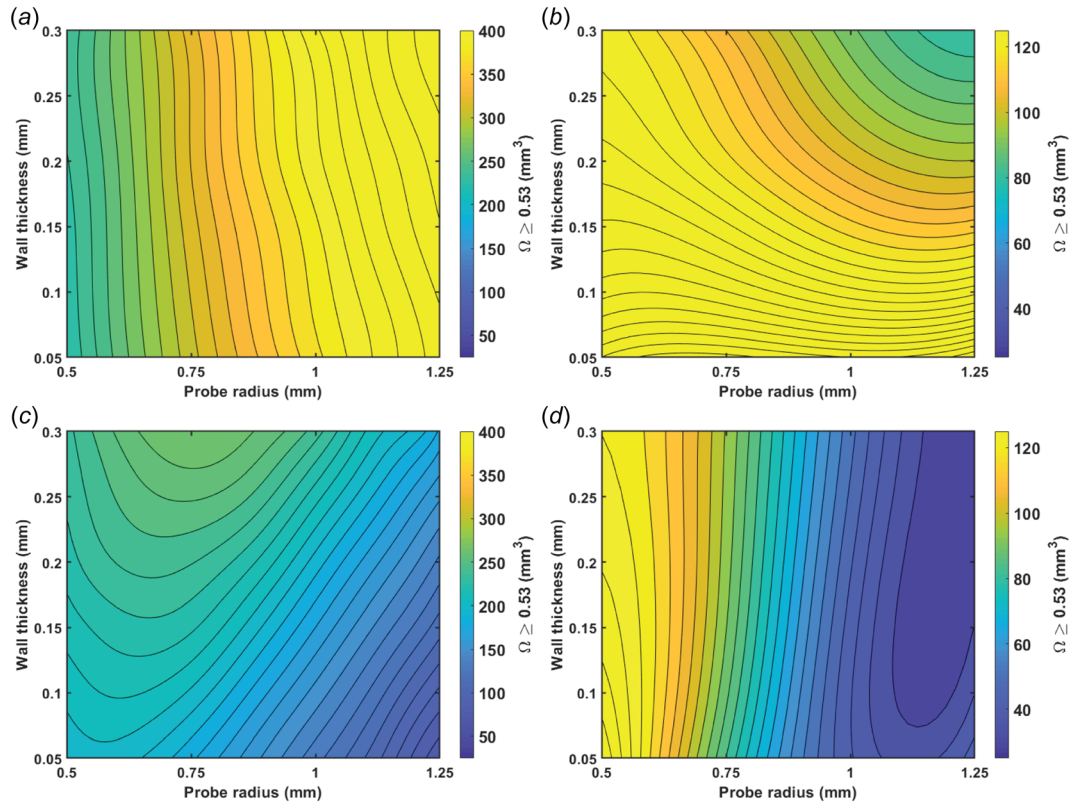
Fig. 6 Impact of probe diameter and wall thickness on thermal damage accumulation for PCM-filled probes relative to solid probes. Volume of tissue undergoing thermal damage ($\Omega \geq 0.53$) 2 min after treatment completion is shown for (*a*) and (*b*) solid probes and (*c*) and (*d*) PCM-filled probes in either a (*a*) and (*c*) bipolar or (*b*) and (*d*) monopolar configuration. Note different y-axis scales for (*a*) and (*c*) bipolar versus (*b*) and (*d*) monopolar cases.
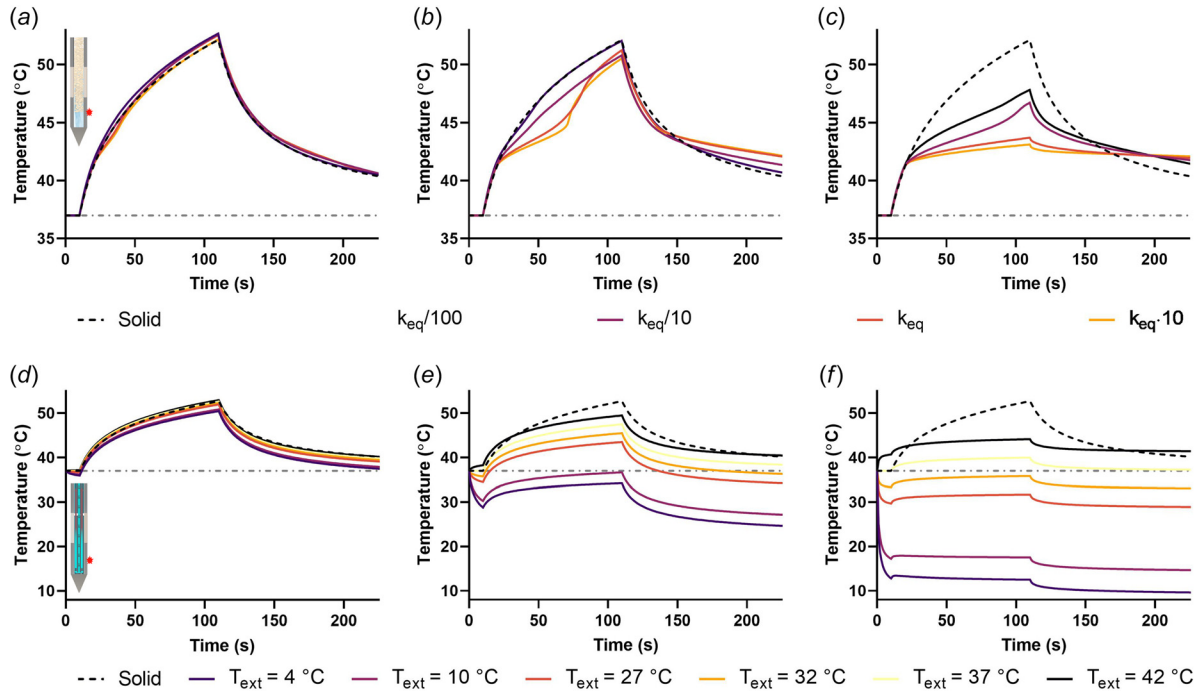

Fig. 7 Performance of PCM-core and actively cooled probes depends upon material properties and user-defined settings. Temperature development during and after pulsing at the vertical midpoint of the distal electrode boundary is shown for (*a*)–(*c*) a PCM-core and (*d*)–(*f*) actively cooled bipolar probe. For PCM-core models, the latent heat of fusion was set to (*a*) $\lambda/10$, (*b*) λ, and (*c*) $\lambda \cdot 10$, respectively, with each curve corresponding to a different effective thermal conductivity (k_{eq}). For actively cooled models, the heat transfer coefficient was varied between (*d*) $h/100$, (*e*) $h/10$, and (*f*) h, respectively. For PCM-core probes, Ø was set to 2 mm while Ø = 1.65 mm was used for actively cooled probes.

solid probes (data not shown). Thus, future efforts should be devoted to quantifying ablative effects of actively cooled probes under the influence of relevant parameters.

Despite the apparent advantages of actively cooled electrodes, this technology is not without limitation. For example, using an actively cooled electrode system requires an external peristaltic pump to circulate perfusate through the probe and the ability to regulate perfusate temperature if desired. Additionally, the probes are heavier and more cumbersome due to the need for external tubing, so additional fixation devices may be necessary to hold the probe(s) in place. In specific instances such as prostate ablation, this may be less concerning since a brachytherapy grid is used to precisely place the IRE probes, stabilizers are already in use for ultrasound transducer positioning, and the probes only need to be inserted a few centimeters [46]. In addition, actively cooled probes may offer further advantages since the prostate is highly conductive (i.e., increased thermal effects) and dense with sensitive vasculature and neural components [47–49]. For other deep-seated or less conductive tumors in which a small amount of thermal damage is acceptable, PCM-core probes might be the preferred option.

Probes with integrated PCM within the core acted to only moderately limit temperature rise as compared to solid electrodes. This effect was heavily dependent upon both the chosen pulse parameters and the probe geometry. With high pulse rates, the PCM completely melted, and temperature increased faster than in the solid case for a few seconds shortly thereafter. Thus, if possible, treatment should be completed prior to PCMs completely undergoing their phase transition. Intuitively, the most effective probe geometries were those that maximized PCM volume (i.e., large radius and thin wall). Probes with diameters of 2 mm or more obviously reduced the peak temperature at the end of treatment by 2–3 °C. Interestingly, despite these seemingly modest effects, the cumulative suppression of temperature development over the course of treatment resulted in substantial reductions of thermal damage (by 40% or more). Because thermal damage depends not only on temperature but also time of exposure, the steady 1–5 °C reduction in temperature over the course of 100 s played a major role in mitigating thermal injury (Figs. 4 and 6).

For comparative purposes, we chose a salt hydrate PCM as originally modeled by Arena and colleagues [30]. However, a wide array of materials could be selected as the PCM within probes used for IRE, with each exhibiting a unique melting point, thermal conductivity, density, and heat of fusion. Each of these characteristics contributes to the behavior of the PCM and its ability to prevent temperature development in different scenarios. For IRE and PEF-based applications, the ideal PCM would have a high density and latent heat of storage to allow the PCM to absorb as much heat as possible given the limited volume of material that can be stored within a needle electrode. Finally, a high thermal conductivity would allow the PCM to conduct heat from the distal region of the probe through the shaft, dispersing the thermal energy among the entire volume of PCM and increasing its effectiveness. Ideally, the phase transition should be initiated as early as possible during treatment, but not completed prior to treatment cessation. This could be tuned by selecting a PCM with an optimal melting temperature. For long duration or high amplitude treatments, the ideal T_m is likely to be 5–10 °C above physiologic temperature. For nonablative treatments such as ECT and EGT, T_m should be just above 37 °C since only a few pulses are administered. For treatment of superficial tissues where probe bodies are not inserted deeply, it may be ideal for T_m to lie near the midpoint of physiological and room temperature. Attractive PCMs include salt hydrates (as studied here) or metallic PCMs, but some eutectics may also be desirable. A number of works comprehensively summarize PCMs available for different applications [50–52].

This paper is intended to directly compare engineered thermal mitigation strategies, but it is important to highlight limitations to the approach employed. First, a 3D model was used to simulate the monopolar configuration, whereas a 2D axisymmetric numerical model was employed to simulate bipolar probes. While this approach significantly reduced computation time, minor differences may exist in the element shape and number between the bipolar and monopolar models, which could have a small impact on the calculated thermal effects. Additionally, we assumed the electrical and thermal properties of pancreatic tissue for this study since IRE is commonly employed for the treatment of unresectable pancreatic adenocarcinoma, and the pancreas is highly sensitive to thermal damage. Thus, while the trends reported in this paper are likely similar for other tissue types, the degree of temperature development for other organ systems will depend upon tissue-specific characteristics such as electrical conductivity, heat capacity, thermal conductivity, and extent of blood perfusion. It is also important to reiterate that TM strategies help reduce the risk of thermal injury within the immediate vicinity of the electrodes. However, certain scenarios may arise where more Joule heating occurs outside the region of influence of either integrated TM strategy. This is conceivable particularly for electrode setups designed to expose large tissue volumes to elevated field strengths [53,54].

Conclusion

Irreversible electroporation is a focal tissue ablation modality used to treat a variety of solid tumors and cardiac arrhythmias. Though cell death occurs predominantly via nonthermal processes, Joule heating can arise in the vicinity of electrodes due to the nonlinear electric field distribution. Integrated thermal mitigation strategies including active cooling and phase change materials have been introduced to limit thermal effects. Here, we numerically studied different clinical and engineered parameters that can affect the performance of thermal mitigation modalities. Our data indicate that probes with either technology will limit thermal damage. Performance of probes with PCM cores is highly dependent upon the properties of the PCM, applied pulse parameters, and probe design choices. Conversely, active cooling efficiently mitigates thermal damage regardless of probe size or applied pulse parameters and can be tuned to maintain tissue temperature at a predetermined value. Because PCM-core probes are less cumbersome and likely more cost-effective compared to actively cooled probes, it is important to consider the drawbacks relative to the benefits of each system compared to existing IRE probes for specific case use.

Nomenclature

AC = active cooling
ECT = electrochemotherapy
EGT = electrogene transfer
IRE = irreversible electroporation
PCM = phase change material
PEF = pulsed electric field
PFA = pulsed field ablation
T = temperature

TM = thermal mitigation

TMP = transmembrane potential

References

[1] Geboers, B., Scheffer, H. J., Graybill, P. M., Ruarus, A. H., Nieuwenhuizen, S., Puijk, R. S., van den Tol, P. M., Davalos, R. V., Rubinsky, B., de Gruijl, T. D., Miklavčič, D., and Meijerink, M. R., 2020, "High-Voltage Electrical Pulses in Oncology: Irreversible Electroporation, Electrochemotherapy, Gene Electrotransfer, Electrofusion, and Electroimmunotherapy," Radiology, **295**(2), pp. 254–272.

[2] Maor, E., Sugrue, A., Witt, C., Vaidya, V. R., DeSimone, C. V., Asirvatham, S. J., and Kapa, S., 2019, "Pulsed Electric Fields for Cardiac Ablation and Beyond: A State-of-the-Art Review," Hear. Rhythm, **16**(7), pp. 1112–1120.

[3] Weaver, J. C., Smith, K. C., Esser, A. T., Son, R. S., and Gowrishankar, T. R., 2012, "A Brief Overview of Electroporation Pulse Strength-Duration Space: A Region Where Additional Intracellular Effects Are Expected," Bioelectrochemistry, **87**, pp. 236–243.

[4] Yarmush, M. L., Golberg, A., Serša, G., Kotnik, T., and Miklavčič, D., 2014, "Electroporation-Based Technologies for Medicine: Principles, Applications, and Challenges," Annu. Rev. Biomed. Eng., **16**(1), pp. 295–320.

[5] Brock, R. M., Beitel-White, N., Davalos, R. V., and Allen, I. C., 2020, "Starting a Fire Without Flame: The Induction of Cell Death and Inflammation in Electroporation-Based Tumor Ablation Strategies," Front. Oncol., **10**, p. 1235.

[6] Batista Napotnik, T., Polajžer, T., and Miklavčič, D., 2021, "Cell Death Due to Electroporation—A Review," Bioelectrochemistry, **141**, p. 107871.

[7] Maor, E., Ivorra, A., Leor, J., and Rubinsky, B., 2007, "The Effect of Irreversible Electroporation on Blood Vessels," Technol. Cancer Res. Treat., **6**(4), pp. 307–312.

[8] Li, W., Fan, Q., Ji, Z., Qiu, X., and Li, Z., 2011, "The Effects of Irreversible Electroporation (IRE) on Nerves," PLoS One, **6**(4), p. e18831.

[9] Vogel, J. A., Van Veldhuisen, E., Agnass, P., Crezee, J., Dijk, F., Verheij, J., Van Gulik, T. M., Meijerink, M. R., Vroomen, L. G., Van Lienden, K. P., and Besselink, M. G., 2016, "Time-Dependent Impact of Irreversible Electroporation on Pancreas, Liver, Blood Vessels and Nerves: A Systematic Review of Experimental Studies," PLoS One, **11**(11), p. e0166987.

[10] Narayanan, G., Bhatia, S., Echenique, A., Suthar, R., Barbery, K., and Yrizarry, J., 2014, "Vessel Patency Post Irreversible Electroporation," Cardiovasc. Intervent. Radiol., **37**(6), pp. 1523–1529.

[11] Muthalaly, R. G., John, R. M., Schaeffer, B., Tanigawa, S., Nakamura, T., Kapur, S., Zei, P. C., Epstein, L. M., Tedrow, U. B., Michaud, G. F., Stevenson, W. G., and Koplan, B. A., 2018, "Temporal Trends in Safety and Complication Rates of Catheter Ablation for Atrial Fibrillation," J. Cardiovasc. Electrophysiol., **29**(6), pp. 854–860.

[12] Narayanan, G., Hosein, P. J., Arora, G., Barbery, K. J., Froud, T., Livingstone, A. S., Franceschi, D., Rocha Lima, C. M., and Yrizarry, J., 2012, "Percutaneous Irreversible Electroporation for Downstaging and Control of Unresectable Pancreatic Adenocarcinoma," J. Vasc. Interv. Radiol., **23**(12), pp. 1613–1621.

[13] Martin, R. C. G., Kwon, D., Chalikonda, S., Sellers, M., Kotz, E., Scoggins, C., McMasters, K. M., and Watkins, K., 2015, "Treatment of 200 Locally Advanced (Stage III) Pancreatic Adenocarcinoma Patients With Irreversible Electroporation Safety and Efficacy," Ann. Surg., **262**(3), pp. 486–492.

[14] Davalos, R. V., Mir, L. M., and Rubinsky, B., 2005, "Tissue Ablation With Irreversible Electroporation," Ann. Biomed. Eng., **33**(2), pp. 223–231.

[15] Garcia, P. A., Rossmeisl, J. H., Neal, R. E., Ellis, T. L., and Davalos, R. V., 2011, "A Parametric Study Delineating Irreversible Electroporation From Thermal Damage Based on a Minimally Invasive Intracranial Procedure," Biomed. Eng. Online, **10**, p. 34.

[16] Cindric, H., Mariappan, P., Beyer, L., Wiggermann, P., Moche, M., Miklavcic, D., and Kos, B., 2021, "Retrospective Study for Validation and Improvement of Numerical Treatment Planning of Irreversible Electroporation Ablation for Treatment of Liver Tumors," IEEE Trans. Biomed. Eng., **68**(12), pp. 3513–3524.

[17] Philips, P., Hays, D., and Martin, R. C. G., 2013, "Irreversible Electroporation Ablation (IRE) of Unresectable Soft Tissue Tumors: Learning Curve Evaluation in the First 150 Patients Treated," PLoS One, **8**(11), p. e76260.

[18] Agnass, P., van Veldhuisen, E., van Gemert, M. J. C., van der Geld, C. W. M., van Lienden, K. P., van Gulik, T. M., Meijerink, M. R., Besselink, M. G., Kok, H. P., and Crezee, J., 2020, "Mathematical Modeling of the Thermal Effects of Irreversible Electroporation for In Vitro, In Vivo, and Clinical Use: A Systematic Review," Int. J. Hyperth., **37**(1), pp. 486–505.

[19] Ansari, D., Kristoffersson, S., Andersson, R., and Bergenfeldt, M., 2017, "The Role of Irreversible Electroporation (IRE) for Locally Advanced Pancreatic Cancer: A Systematic Review of Safety and Efficacy," Scand. J. Gastroenterol., **52**(11), pp. 1165–1171.

[20] Dunki-Jacobs, E. M., Philips, P., and Martin, R. C. G., 2014, "Evaluation of Thermal Injury to Liver, Pancreas and Kidney During Irreversible Electroporation in an In Vivo Experimental Model," Br. J. Surg., **101**(9), pp. 1113–1121.

[21] Wandel, A., Ben-David, E., Ulusoy, B. S., Neal, R., Faruja, M., Nissenbaum, I., Gourovich, S., and Goldberg, S. N., 2016, "Optimizing Irreversible Electroporation Ablation With a Bipolar Electrode," J. Vasc. Interv. Radiol., **27**(9), pp. 1441–1450.e2.

[22] Buist, T. J., Groen, M. H. A., Wittkampf, F. H. M., Loh, P., Doevendans, P. A. F. M., Van Es, R., and Elvan, A., 2021, "Efficacy of Multi-Electrode Linear Irreversible Electroporation," Europace, **23**(3), pp. 464–468.

[23] O'Brien, T. J., Lorenzo, M. F., Zhao, Y., Neal, R. E., II, Robertson, J. L., Goldberg, S. N., and Davalos, R. V., 2019, "Cycled Pulsing to Mitigate Thermal Damage for Multi-Electrode Irreversible Electroporation Therapy," Int. J. Hyperth., **36**(1), pp. 953–963.

[24] Ren, F., Li, Q., Gao, X., Zhu, K., Zhang, J., Chen, X., Yan, X., Chu, D., Hu, L., Gao, Z., Wu, Z., Wu, R., and Lv, Y., 2019, "Electrical and Thermal Analyses of Catheter-Based Irreversible Electroporation of Digestive Tract," Int. J. Hyperth., **36**(1), pp. 854–867.

[25] Yang, Y., Moser, M., Zhang, E., Zhang, W., and Zhang, B., 2018, "Optimization of Electrode Configuration and Pulse Strength in Irreversible Electroporation for Large Ablation Volumes Without Thermal Damage," ASME J. Eng. Sci. Med. Diagnost. Ther., **1**(2), p. 021002.

[26] Shao, Q., O'Flanagan, S., Lam, T., Roy, P., Pelaez, F., Burbach, B. J., Azarin, S. M., Shimizu, Y., and Bischof, J. C., 2019, "Engineering T Cell Response to Cancer Antigens by Choice of Focal Therapeutic Conditions," Int. J. Hyperth., **36**(1), pp. 130–138.

[27] Zhao, J., Wen, X., Tian, L., Li, T., Xu, C., Wen, X., Melancon, M. P., Gupta, S., Shen, B., Peng, W., and Li, C., 2019, "Irreversible Electroporation Reverses Resistance to Immune Checkpoint Blockade in Pancreatic Cancer," Nat. Commun., **10**(1), p. 899.

[28] Beitel-White, N., Martin, R. C. G., Li, Y., Brock, R. M., Allen, I. C., and Davalos, R. V., 2019, "Real-Time Prediction of Patient Immune Cell Modulation During Irreversible Electroporation Therapy," Sci. Rep., **9**(1), p. 17739.

[29] O'Brien, T. J., Bonakdar, M., Bhonsle, S., Neal, R. E., Aardema, C. H., Robertson, J. L., Goldberg, S. N., and Davalos, R. V., 2018, "Effects of Internal Electrode Cooling on Irreversible Electroporation Using a Perfused Organ Model," Int. J. Hyperth., **35**(1), pp. 44–55.

[30] Arena, C. B., Mahajan, R. L., Rylander, M. N., and Davalos, R. V., 2012, "Towards the Development of Latent Heat Storage Electrodes for Electroporation-Based Therapies," Appl. Phys. Lett., **101**(8), p. 083902.

[31] Arena, C. B., Mahajan, R. L., Nichole Rylander, M., and Davalos, R. V., 2013, "An Experimental and Numerical Investigation of Phase Change Electrodes for Therapeutic Irreversible Electroporation," ASME J. Biomech. Eng., **135**(11), p. 111009.

[32] Zhao, Y., and Davalos, R. V., 2020, "Development of an Endothermic Electrode for Electroporation-Based Therapies: A Simulation Study," Appl. Phys. Lett., **117**(14), pp. 143702–5.

[33] Garcia, P. A., Davalos, R. V., and Miklavcic, D., 2014, "A Numerical Investigation of the Electric and Thermal Cell Kill Distributions in Electroporation-Based Therapies in Tissue," PLoS One, **9**(8), e103083.

[34] Davalos, R. V., and Rubinsky, B., 2008, "Temperature Considerations During Irreversible Electroporation," Int. J. Heat Mass Transfer, **51**(23–24), pp. 5617–5622.

[35] Mohammadi, A., Bianchi, L., Asadi, S., and Saccomandi, P., 2021, "Measurement of Ex Vivo Liver, Brain and Pancreas Thermal Properties as Function of Temperature," Sensors, **21**(12), p. 4236.

[36] Garcia, P. A., Pearce, J. A., and Davalos, R. V., 2012, "A Comparison Between the Pulsed and Duty Cycle Approaches Used to Capture the Thermal Response of Tissue During Electroporation-Based Therapies," ASME Paper No. SBC 2012.

[37] Diller, K. R., and Hayes, L. J., 1983, "A Finite Element Model of Burn Injury in Blood–Perfused Skin," ASME J. Biomech. Eng., **105**(3), pp. 300–307.

[38] Beitel-White, N., Lorenzo, M. F., Zhao, Y., Brock, R., Coutermarsh-Ott, S., Allen, I. C., Manuchehrabadi, N., and Davalos, R. V., 2021, "Multi-Tissue Analysis on the Impact of Electroporation on Electrical and Thermal Properties," IEEE Trans. Biomed. Eng., **68**(3), pp. 771–782.

[39] Ngo, I. L., Jeon, S., and Byon, C., 2016, "Thermal Conductivity of Transparent and Flexible Polymers Containing Fillers: A Literature Review," Int. J. Heat Mass Transfer, **98**, pp. 219–226.

[40] Hasgall, P., Di Gennaro, F., Baumgartner, C., Neufeld, E., Lloyd, B., Gosselin, M., Payne, D., Klingenböck, A., and Kuster, N., 2021, "IT'IS Database for Thermal and Electromagnetic Parameters of Biological Tissues," Version 4.0, May 15, 2018.

[41] O'brien, T. J., 2019, "An Investigation of Thermal Mitigation Strategies for Electroporation-Based Therapies," Ph.D. dissertation, Virginia Tech.

[42] Liu, D., and Yu, L., 2010, "Experimental Investigation of Single-Phase Convective Heat Transfer of Nanofluids in a Minichannel," ASME Paper No. IHTC14-23018.

[43] Jourabchi, N., Beroukhim, K., Tafti, B. A., Kee, S. T., and Lee, E. W., 2014, "Irreversible Electroporation (NanoKnife) in Cancer Treatment," Gastrointest. Interv., **3**(1), pp. 8–18.

[44] Sano, M. B., Fesmire, C. C., and Petrella, R. A., 2021, "Electro-Thermal Therapy Algorithms and Active Internal Electrode Cooling Reduce Thermal Injury in High Frequency Pulsed Electric Field Cancer Therapies," Ann. Biomed. Eng., **49**, pp. 191–202.

[45] Edelblute, C. M., Hornef, J., Burcus, N. I., Norman, T., Beebe, S. J., Schoenbach, K., Heller, R., Jiang, C., and Guo, S., 2017, "Controllable Moderate Heating Enhances the Therapeutic Efficacy of Irreversible Electroporation for Pancreatic Cancer," Sci. Rep., **7**(1), p. 11767.

[46] Baur, D. J., Collettini, F., Enders, J., Maxeiner, A., Schreiter, V., Stephan, C., Gebauer, B., Hamm, B., and Fischer, T., 2017, "MRI-TRUS Fusion for Electrode Positioning During Irreversible Electroporation for Treatment of Prostate Cancer," Diagnos. Interv. Radiol., **23**(4), pp. 321–325.

[47] Neal, R. E., Millar, J. L., Kavnoudias, H., Royce, P., Rosenfeldt, F., Pham, A., Smith, R., Davalos, R. V., and Thomson, K. R., 2014, "In Vivo Characterization and Numerical Simulation of Prostate Properties for Non-Thermal Irreversible Electroporation Ablation," Prostate, **74**(5), pp. 458–468.

[48] Campelo, S., Valerio, M., Ahmed, H. U., Hu, Y., Arena, S. L., Neal, R. E., Emberton, M., and Arena, C. B., 2017, "An Evaluation of Irreversible

Electroporation Thresholds in Human Prostate Cancer and Potential Correlations to Physiological Measurements," APL Bioeng., **1**(1), p. 016101.

[49] Checcucci, E., Amparore, D., De Luca, S., Autorino, R., Fiori, C., and Porpiglia, F., 2019, "Precision Prostate Cancer Surgery: An Overview of New Technologies and Techniques," Minerva Urol. Nefrol., **71**(5), pp. 487–501.

[50] Su, W., Darkwa, J., and Kokogiannakis, G., 2015, "Review of Solid-Liquid Phase Change Materials and Their Encapsulation Technologies," Renewable Sustainable Energy Rev., **48**, pp. 373–391.

[51] Jankowski, N. R., and McCluskey, F. P., 2014, "A Review of Phase Change Materials for Vehicle Component Thermal Buffering," Appl. Energy, **113**, pp. 1525–1561.

[52] Zalba, B., Marín, J. M., Cabeza, L. F., and Mehling, H., 2003, "Review on Thermal Energy Storage With Phase Change: Materials, Heat Transfer Analysis and Applications," Appl. Therm. Eng., **23**(3), pp. 251–283.

[53] Kaufman, J. D., Fesmire, C. C., Petrella, R. A., Fogle, C. A., Xing, L., Gerber, D., and Sano, M. B., 2020, "High-Frequency Irreversible Electroporation Using 5,000-V Waveforms to Create Reproducible 2- and 4-Cm Ablation Zones—a Laboratory Investigation Using Mechanically Perfused Liver," J. Vasc. Interv. Radiol., **31**(1), pp. 162–168.

[54] Zhao, Y., McKillop, I. H., and Davalos, R. V., 2021, "Modeling of a Single Bipolar Electrode With Tines for Irreversible Electroporation Delivery," Comput. Biol. Med., p. 104870.